Nuclear Materials and Energy 46 (2026) 102071

Contents lists available at ScienceDirect

Nuclear Materials and Energy

journal homepage: www.elsevier.com/locate/nme

Imaging analysis of ps laser induced ablation spectroscopy and mass spectrometry – deuterium depth resolution, removal fraction, and uncertainties

Sören Möller [a,*], Christoph Kawan [b,d], Marcin Rasinski [b], Gennady Sergienko [b], Arkadi Kreter [b], Eduard Grigore [c], Erik Wüst [b,d], Khoirul Faiq Muzakka [a], Sebastijan Brezinsek [b]

[a] Forschungszentrum Jülich GmbH, Institute of Energy Materials and Devices - Materials Synthesis and Processing, Jülich, Germany
[b] Forschungszentrum Jülich GmbH, Institute of Fusion Energy and Nuclear Waste Management – Plasma Physics, Partner of the Trilateral Euregio Cluster (TEC), Jülich, Germany
[c] Plasma Physics and Nuclear Fusion Department, National Institute for Laser, Plasma and Radiation Physics, Magurele City, Romania
[d] Mathematisch- Naturwissenschaftliche Fakultät, HHU Düsseldorf, Düsseldorf, Germany

ARTICLE INFO

Keywords:
Nuclear fusion
Nuclear materials
LIBS
LIA
Ion-beam analysis
Tungsten
Surface analysis
Deuterium retention

ABSTRACT

Laser based surface composition analysis methods are used as an in-situ tool for material analysis in nuclear fusion reactors. The methods investigated here ablate material from the surface and analyse the surface composition through the released particles. A quantification requires the calibration of the detection efficiency of the released material and its relation to the affected surface area and depth. Only with this quantification, the laser methods can provide quantitative data on hydrogen isotope retention and plasma-surface interaction.

In this work, we combine three high-resolution imaging techniques to provide a complete understanding of the surface structure and elemental composition using a ps-Laser ablating ~5 μm of W. MeV ion-beam analysis (IBA), in particular with the latest developments regarding high-throughput IBA imaging provides insight into the deuterium content. This enables a new and unique experimental insight into five individual limitations of the deuterium depth resolution and accuracy limitations of laser ablation methods related to the matrix effect. The results enable precise calibration of laser methods and understanding of their limitations. In particular, the thermal desorption halo, the crater-floor depletion fraction, and the impact of crater edge effects are quantified. From sample effect, we see a relative uncertainty of ±9% and an absolute uncertainty of ±52%.

Introduction

Nuclear fusion research is strongly connected to the question of hydrogen isotope retention, since deuterium and tritium are considered for fuelling the fusion reactions. If this hydrogen is implanted into surfaces and retained in materials, it cannot be used for the fusion reactions. Therefore, analysing the retained amounts is crucial for quantifying the problem and finding strategies to mitigate it.

The in-situ analysis in a fusion device (or any other vacuum vessel) is possible through laser-induced ablation (LIA) [1,2]. A high power density laser irradiates the surface to be analysed, releasing material through ablation and desorption processes. Subsequent analysis of the released material through spectroscopy and mass spectrometry enables quantifying the target composition in terms of the hydrogen isotope content and other elements. LIA can probe the elemental depth profiles (EDP) through multiple pulses ablating on the same location. Both, the depth and the concentration analysis require calibration in order to quantify the EDP. The many processes involved in LIA complicate this calibration, since it requires exact knowledge of the affected area and the fraction of released material. The ablation can result in surface roughening and grain orientation dependent ablation, depending on the laser properties. The laser energy is deposited in a short time (typically on the fs or ps scale) but it still heats up the material leading to melting and outgassing. The combination of the sample related effects is called matrix effect and represents the main challenge in absolute LIA analysis.

MeV Ion-Beam Analysis (IBA) is a powerful analysis method used in plasma-surface interaction studies and many other fields [3–5]. It can provide sub-mm resolved imaging of elemental and isotopic

* Corresponding author.
E-mail address: s.moeller@fz-juelich.de (S. Möller).

https://doi.org/10.1016/j.nme.2026.102071
Received 25 November 2025; Received in revised form 19 January 2026; Accepted 23 January 2026
Available online 26 January 2026

concentrations. Therefore, it is widely used as a post-mortem analysis method in combination with laser based analysis method enabling calibration of the obtained signal. In this work, we extend this connection through recent advances in large-area and high point-density IBA imaging. This enables a deeper understanding of the affected area and the released material fraction. Finally, a generalisation of LIA effects could be provided through IBA in order to find universal calibration factors and understand the application limits and best practices of LIA.

Methods

The sample is prepared with a 4.6 μm W (measured by confocal profilometry at the layer edge) physical vapour deposited layer on a pure 10x10x5 mm^3 Mo substrate. The W coating was deposited by magnetron sputtering at the National Institute for Laser, Plasma & Radiation Physics (INFLPR), Romania. Before deposition the sample was polished to mirror finish ($R_a \leq 15$ nm) This material is exposed in PSI-2 [6] D_2 plasma at 820 K to a fluence of $7*10^{25}$ D/m^2 in order to saturate the W layer with D. An earlier study used this sample type before [6]. The samples are stored at room temperature for ~ 1 year making dynamic outgassing negligible.

The LIA analysis of this samples is published separately [7] and one of the results is reproduced in Fig. 1 a). The sample is used for multiple different LIA points related to other studies. The smaller 0.1 mm spots are not considered here, but will be visible between the lasers LIA points investigated here. For these larger points, a 35 ps laser with 355 nm wavelength and 20 mJ pulse energy focused to 0.85 mm diameter spot-size (0.567 mm^2), determined by a laser profilometer, was used in a vacuum setup. The spot diameter is determined using a laser-profiling device. This results in an ablation rate of about 15 nm per pulse. A few hundred pulses (~300) were shot on every LIA point in order to fully ablate the W layer.

IBA uses a 2950 ± 20 keV ^{3}He ion beam with 10–20 nA current sample from a 1.7 MV tandem accelerator on the sample. The sample is analysed in the IBA end-station described in [8] and evaluated using SimNRA 7.04 [9] and AutoNRA 1.05 [10]. The automated fitting using AutoNRA is conducted without quadratic calibration term, in order to stabilise the fitting result against detector calibration drifts. While this slightly lowers the accuracy of the depth axis, it is required to enable the fitting of the numerous spectra acquired with high count-rate over the long measurement duration of about 20 h per map. Unfortunately, this leads to a limited offset of the energy calibration of the ^{3}He(D,p)^{4}He peak, resulting in a misinterpretation of the surface-near D concentrations. Two analyses are carried out. First 890 points with 150 μm spot-size and grid-spacing with 2 μC ^{3}He dose per point are carried out on a 5x4.5 mm^2 area, see Fig. 2 a), followed by a magnified analysis with 50 μm spot-size and grid-spacing and 370 points with 1 μC per point, see Fig. 5 a) and Fig. 6. The spot size equals the lateral resolution, while the depth resolution for D is about 1.3 μm. On the small spot size, the beam introduces 12 MW/m^2 of heat, potentially influencing the sample. A negligible impact is seen in the bottom of Fig. 2 b), where the IBA spots are visualised in the deposits outside the LIA craters. The initial D retention accounts to $602 \pm 20 \times 10^{19}$ $/m^2$ and is limited to the W layer. IBA shows that this D is distributed mostly evenly throughout the W layer depth see Fig. 1 b). From IBA we can determine a W layer thickness of 3.5 μm assuming pure W with 100% density equal to 0.158 nm/(10^{19} W/m^2). Up to 98.5% of the initial D is released in some locations of the crater floor, but a significant part of the crater floor contains more D. In the crater area in total an average of 17 ± 2% of the deuterium originally present in the layer is remaining. This fraction varies strongly locally, ranging from 1.5% to 52%.

For the post-mortem analysis, profilometry using a STIL Micromesure 2 laser profilometer is conducted after IBA. The analysis yields light reflectivity Fig. 2 b) and height profiles Fig. 5 b) of the sample surface. We expect an effective lateral resolution of 10 μm and a depth resolution of 10 nm. Fitting shows a FWHM width of the crater of 825 ± 30 μm and a crater flank width of 13.6 ± 5 μm, see Fig. 3. The total crater area measured at its outer edge is with 0.573 mm^2 about 10% smaller than the nominal area. The diameter and flank width of IBA and laser profilometry agree with each other. The LIA craters show a non-circular shape, although the deviation from a circle is small and reproducible in different craters.

Fig. 5 shows the high-resolution analysis of the laser crater comparing profilometry and the total D-content imaging from IBA. In both analyses, we see several deviations from the LIA assumption of a circular top-hat crater profile. The non-circularity is identically observed in both methods, for example with an extension of the crater towards the 1 o'clock direction.

In order to obtain a meaningful result, the elemental quantification has to be related to the analysed area. The crater edge and its thermal desorption halo represent the main uncertainties in the area calibration. The crater edge steepness is determined through an exponential peak fitting using a double sigmoid function, see equation (1). Here y_0 is the baseline, x_c the x-centre, A the peak height, w_1 the FWHM peak width, and $w_{2,3}$ the edge steepness. This equation yields a HWHM width of the Gaussian edge slope of 16 ± 2 μm corresponding to a total edge width of ~ 32 μm equal to 64 μm when considering the diameter. Compared to the 850 μm crater diameter, which we consider as the diameter

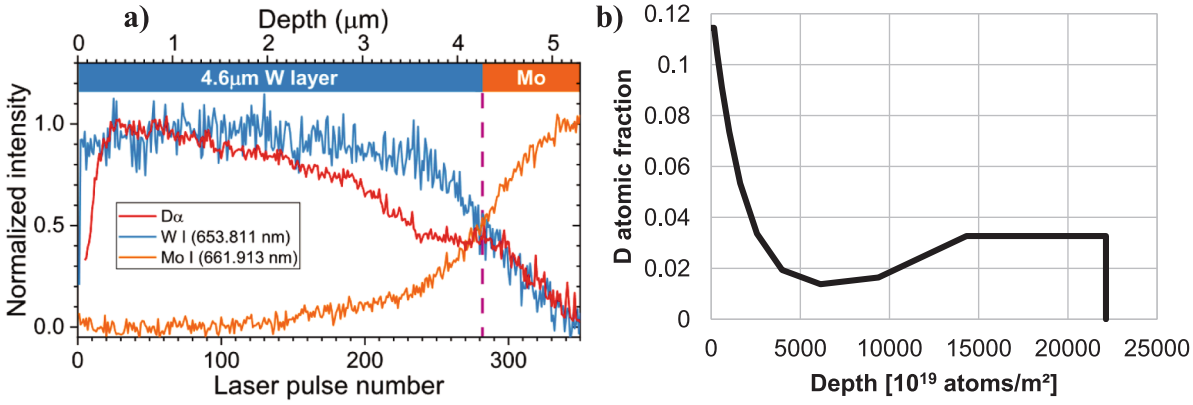

Fig. 1. a) Shows the libs signal evolution with the corresponding d_α signal. LIBS cannot resolve the sharp transition of the W layer boundary in the EDP as IBA can. The formation of surface roughness (influencing D, W, Mo) in and a heat halo (influencing only D) around the laser affected area have significant impact on the LIBS signal and the methods depth resolution. Reproduced from [7] with permission. b) Typical elemental depth profile of D after PSI-2 exposure. The near-surface concentration peak is a fitting effect and the D-EDP can be considered hat-shaped. The probing range of IBA is 27,000 units in this case corresponding to 4.2 μm bulk W.

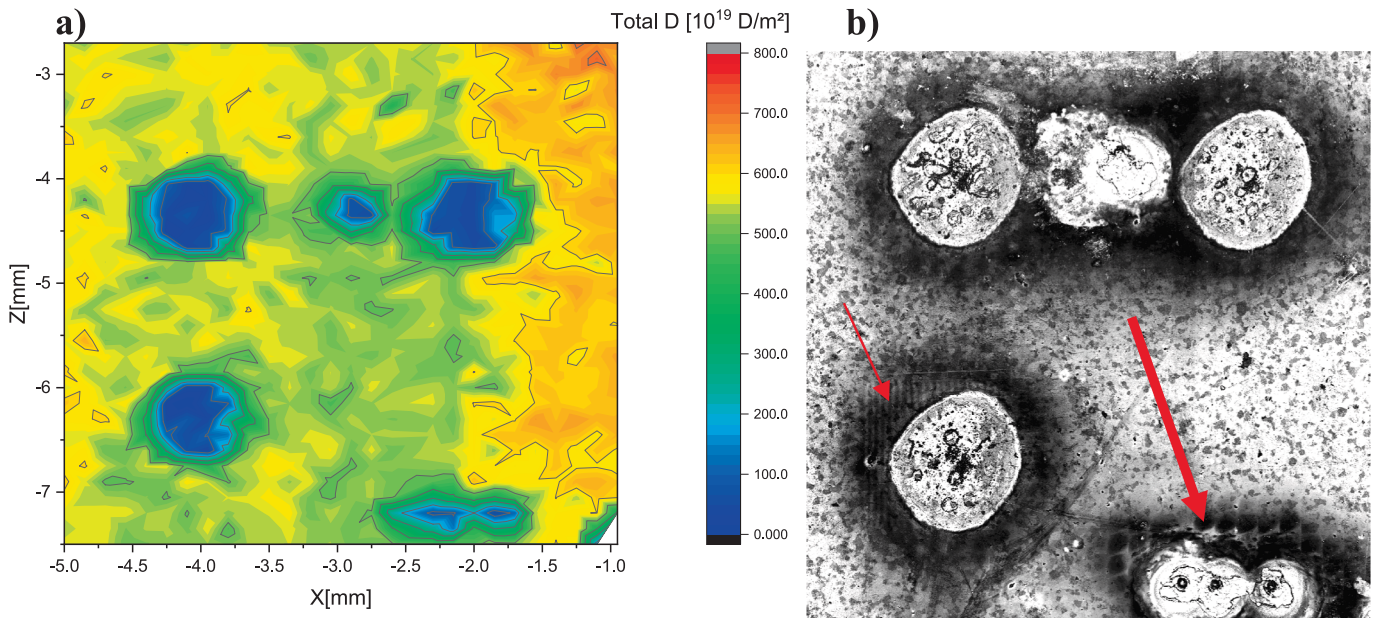

Fig. 2. 5 × 4.5 mm^2 area analysis with 150 μm lateral resolution. It shows 3 laser craters with 1 mm nominal diameter and 4 laser craters with nominal 0.1 mm diameter. The initial D distribution is relatively flat, except for a ~ 20% higher value at the right edge. The right image shows the reflectivity imaging of the laser profilometer. In the dark halos around the spots on the lower right, we can see the imprints of the 150 μm IBA analysis spots and around the large spot on the lower left we can see the small imprints from the 50 μm IBA spots (red arrows guide the eye). (For interpretation of the references to colour in this figure legend, the reader is referred to the web version of this article.)

including the edge, this is a significant number of 14% of the crater surface area.

$$y(x) = y_0 + \frac{A}{1+e^{\frac{-x-x_c+\frac{w_1}{2}}{w_2}}} * \left(1 - \frac{1}{1+e^{\frac{-x-x_c+\frac{w_1}{2}}{w_3}}}\right) \quad (1)$$

The ~0.3 mm dark halo seen around the craters in Fig. 2 b) and Fig. 5 b) is not visible in the D retention Fig. 5 a). Fig. 6 demonstrates the darkening mostly relates to C and O deposition around the crater. The upper left edge of the figures is just outside the dark halo, therefore representing the original C and O content. The O thickness increased from 1 × 10^{21}O/m^2 to 1.6 × 10^{21}O/m^2 and the C thickness from 0.5 × 10^{21}C/m^2 to 1.7 × 10^{21}C/m^2 just outside the crater. Besides this ~20 nm layer of C and O we also see two thick flakes containing C and O in about 0.25 mm distance to the crater edge. The laser ablation removes the surface oxygen inside the crater, but the carbon levels even increase up to 18 × 10^{21}C/m^2. This leads to the question of the origin of the additional C found on the sample. The O could be redistributed from the crater to its surrounding, but the total surface carbon increase requires an external carbon source, e.g. the gas phase or reflected laser light (reflectivity of W ~ 50% [11]) ablating carbon deposits from the stainless steel surfaces of the LIA chamber.

An exemplary D-depth profile obtained at the crater floor is shown in Fig. 7. The W layer is completely removed here, but a small fraction of D remains. Originally no D was present here, as indicated in Fig. 1 b). Therefore, the LIA process has driven a small fraction of the D into the bulk. If this happened through diffusion we would expect an exponential decrease towards the depth. The observed increase suggests diffusion of D into the substrate together with outgassing of the near-surface substrate region due to the laser induced heat down to about 1.8 μm.

Discussion and conclusion

We successfully analysed a tungsten sample with a D retention in the order of 2 at.% using laser ablation, laser profilometry, electron microscopy, and MeV ion-beam analysis imaging. We identified several limitations and uncertainties related to the quantification of the LIA results.

The heat introduced by the ps-laser introduces a thermal halo leading to D outgassing beyond the ablated volume. We observed this halo indirectly through the D-EDP at the crater floor. Originally, this volume was not D loaded, as demonstrated by the initial D-EDP and the complete W layer ablation. Therefore, the detected D can only be transported to this volume through the laser induced thermal diffusion. The thermal halo will strongly influence the signal in the first few μm of LIA ablation, but it can be described through the data presented here and/or thermal outgassing models, which can also consider the material and laser properties. Irradiation damage in a fusion reactor might change the trapping sites and therefore the outgassing temperatures for D and T, altering the size of the effusion halo. Compared to the diameter of 825 μm, the thermal halo is negligible. Compared to the crater depth of about 5 μm, the 1.8 μm halo is significant. In particular, for the typical crater depth in the order of μm, the thermal halo can result in a significant overestimation of the D retention by releasing D from below the ablation depth, while for shallow D retention it is negligible. Furthermore, it limits the effective depth resolution of D analysis to 1.8 μm, in spite of only 15 nm ablation per laser pulse. Consequently, the LIA depth analysis becomes an inverse problem: We have to know the depth profile in order to be able to compensate for its effect on the measured depth signal. Our recommendation is to ablate as deep as possible and assume a parametrisation of the depth profile (e.g. an exponential or a constant) in combination with a thermal modelling of the halo in order to overcome this depth resolution limitation.

The C and O deposition (Fig. 5 a) and Fig. 6) are anti-correlated with the remaining D retention. This is true for the crater floor as well as the debris outside the crater. This indicates only little impact on the uncertainty of LIA for D retention. It could induce irregularities in the EDPs, since the deposits seem to accelerate the local D removal or shield the underlying D from the analysis. This can introduce a noisy behaviour in the LIA depth profile or its consecutive laser pulses, respectively. The strong correlation of C and O speaks against the explosion of sub-surface blisters as the origin of the deposited flakes, but rather supports stray light induced LIA on other surfaces or gas-phase deposition.

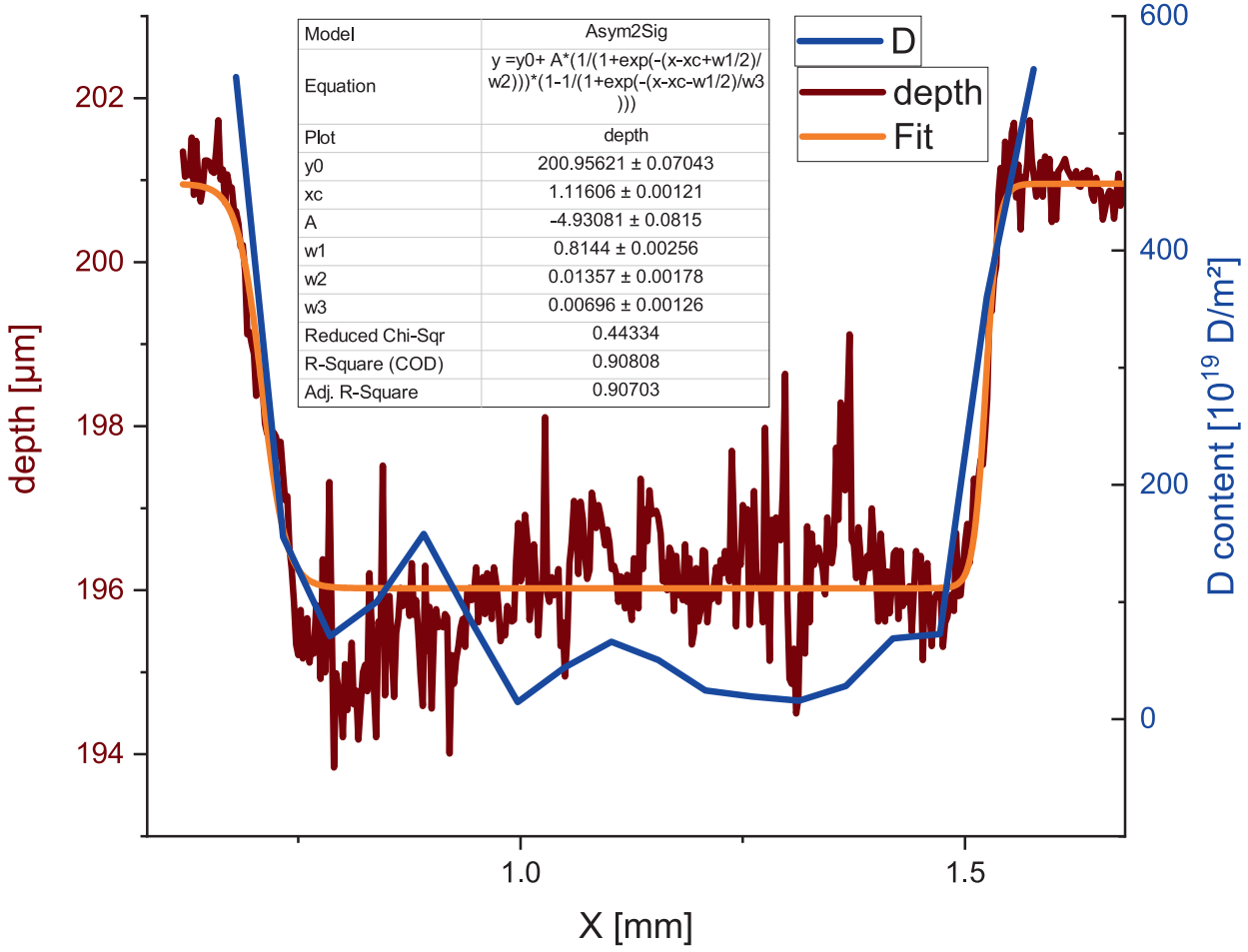

Fig. 3. Vertical profile plots of the laser profilometer (dark red) and the IBA D-retention (blue) on the same line through the laser crater. The profile shapes agree with each other, although the IBA resolution is not as good as the profilometer resolution. Both methods have calibrated coordinates with < 1 µm accuracy. A double sigmoid function describes the shape with $R^2 = 0.9$, which is good considering the roughness. Fitting results using equation: y = y0 + A*(1/(1 + exp(−(x−xc + w1/2)/w2)))*(1–1/(1 + exp(−(x−xc−w1/2)/w3))). y0 = 200.95621 ± 0.07043;xc = 1.11606 ± 0.00121; A = −4.93081 ± 0.0815; w1 = 0.8144 ± 0.00256; w2 = 0.01357 ± 0.00178; w3 = 0.00696 ± 0.00126; Reduced Chi^2 = 0.44334; $R^2 = 0.90808$; Scanning electron microscopy (SEM) and focussed ion beam milling (FIB) are used for high-resolution imaging of the laser surface modifications. These data support the interpretation of the profilometer data by providing additional verification that observed structures are not related to optical properties influencing the profilometer signal, but represent real topographic features. Fig. 4 shows a LIA crater in three different SEM magnifications. The crater is surrounded by an edge zone like in the IBA data. In the inner part of the crater, the formerly flat surface is significantly roughened, featuring several elliptically shaped ridges of pillars. We can only speculate why these structures are formed/remaining. Maybe it is an effect of the W deposit structure, related to O and C deposited from the atmosphere, or a peculiarity of the laser beam. A crosscut of one pillar suggests that it partially preserves the original W-layer thickness with a total height of about 6 µm. It also shows a certain porosity and small grains in the W-layer and the dense, large grain Mo bulk. This potentially means that a part of the W-layer remains unaffected from the LIA process. The outside of the column appears to be covered by a formerly molten layer. In the frame of this work, we cannot determine the fraction of the crater area covered by the pillars. Outside the crater, a few debris-like grains are attached to the surface. (For interpretation of the references to colour in this figure legend, the reader is referred to the web version of this article.)

Consequently, a lower vacuum pressure and shorter laser focal length could help reducing this effect.

The crater floor is seen to feature numerous pillar-like structures. These structures could be responsible for the regions of partial outgassing on the crater floor. This type of structures is not seen in all LIA craters in the literature and might be specific to the investigated layer of laser settings, therefore representing an uncertainty in LIA analysis. The SEM imaging indicates that at least some of the pillars have a height of exceeding the IBA range of 4 µm in W, indicating that there could be more D shielded from LIA by the pillars but not seen in this IBA imaging. Averaged over the 50 µm IBA spot diameter, the outgassed fraction of D varies between 98.5% and 48%, supporting the significant impact of the surface structure. In total 17% of the D originally present in the laser crater area are still detectable with IBA. The melted surface impression of the pillars and their arrangement in about 100 µm sized elliptical structures leaves us puzzled about their origin. The comparison of the three investigated laser craters shows a high degree of reproducibility, but the relevance of the laser and material properties on their development and the related D release fraction remains unclear. Therefore, this pillar D-retention represents a major uncertainty for absolute quantification.

The non-circularity of the laser crater appears to result 10% smaller crater area compared to its laser profilometer determined beam size, limiting the determination e.g. of the areal density of D by LIA. Our analyses yielded a crater edge zone of 64 µm in the diameter in W. This reduces the affected area by another 14%. In particular, for small diameter LIA craters, in particular the crater flank area introduces a significant uncertainty and limitation. The area of LIA spot sizes of ≤ 0.1 mm will be $> 75\%$ dominated by edge effects, making a quantitative interpretation of difficult in this case. The size of about 1 mm diameter will have about 10% uncertainty related to this effect. The observation of exponential edges with a FWHM in the D outgassing of 16 ± 2 µm suggest to correct for the crater flank effect by simply subtracting this FWHM value from the nominal spot diameter for the given laser

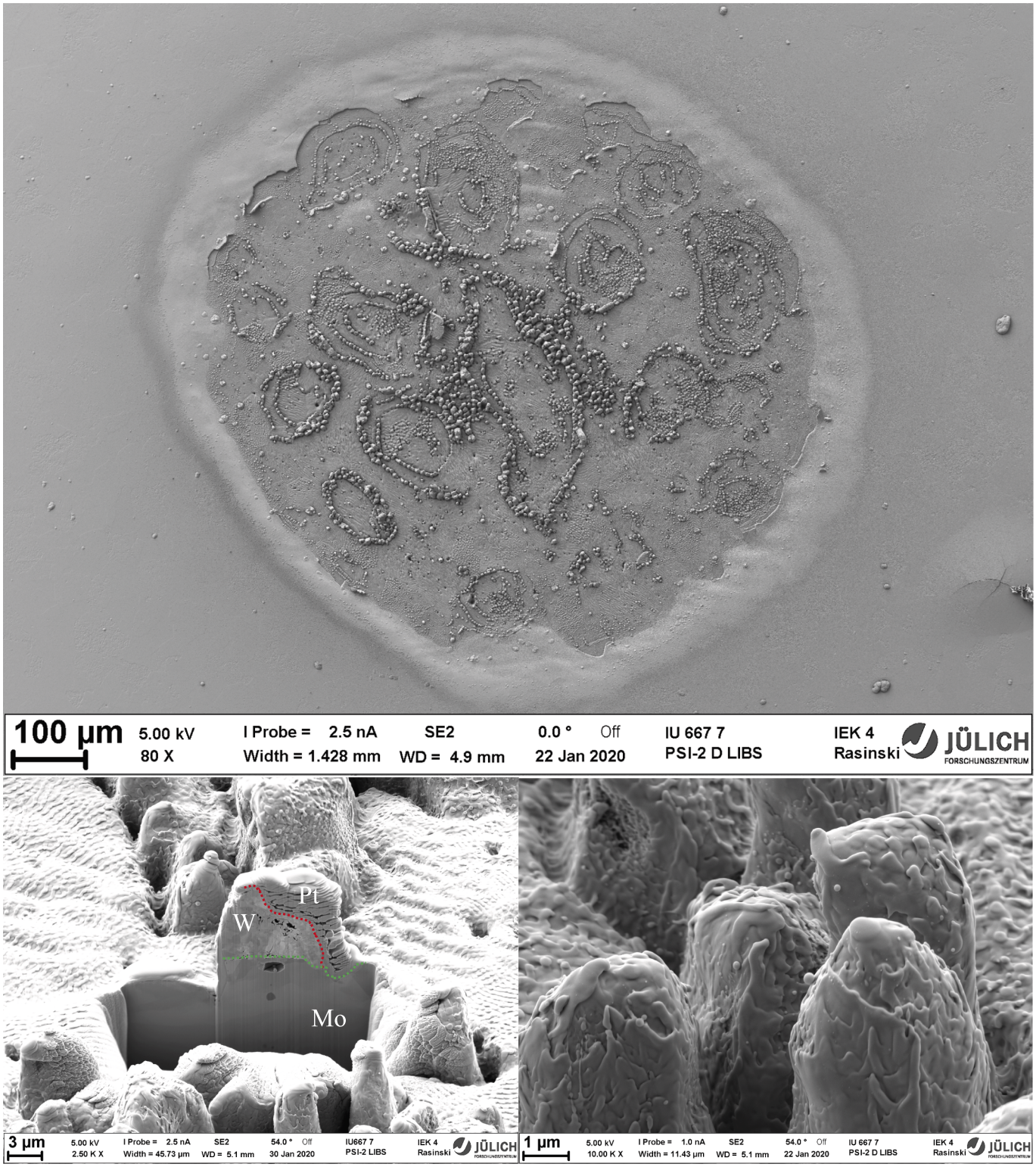

Fig. 4. SEM imaging of the crater after 330 LIA pulses with additional detailed images of the structures developing inside the crater. The crater orientation differs from the other figures shown here by about 180°. The pillar-like feature has a Pt deposition introduced for the FIB process on its right side (right of the red line). The red line marks the edge of the original W layer and the green line the interface to the Mo bulk. The original layer thickness is preserved in a small part of the pillar. The pillar outer surface impression shows melt layer movement. The crosscut pillar extends about 6 µm above the post-laser surface indicated by the different grain size boundary. (For interpretation of the references to colour in this figure legend, the reader is referred to the web version of this article.)

parameters.

The combination of reduced effective area and the D remaining in the crater results in a LIA signal reduction of 34%. The combined error of the crater flank, circularity, thermal halo, pillar retention, and depth diffusion effects yields a total absolute error (=systematic underestimation) for the analysed 0.85 mm laser spot of 52% in the investigated case of an initially shallow D retention compared to the laser ablation thickness. In other words, in the case presented here, the LIA signal has

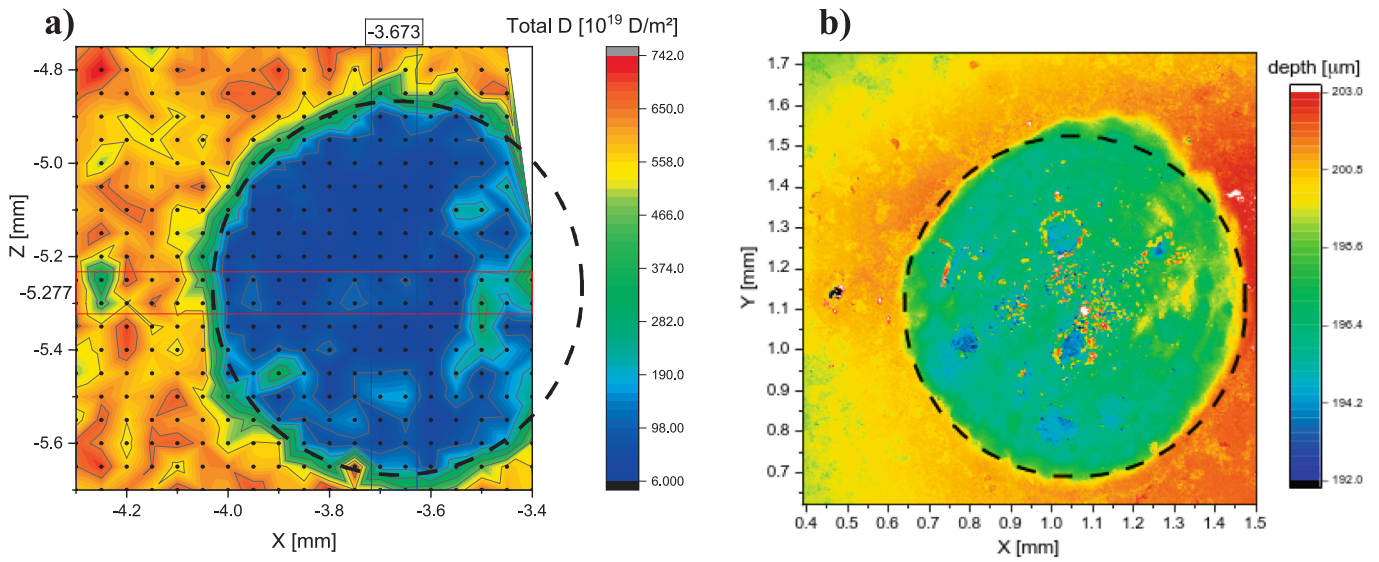

Fig. 5. Analysis of the bottom-left laser spot with higher lateral resolution. The crater has a FWHM size of 0.8 + -0.01 mm (circle). The left image shows the IBA map of the integrated D inventory. The right image shows the corresponding topography using a laser profilometer. The roughness present in the laser crater has a significant impact on the local D removal. The upper left part is completely depleted, but the lower right half shows some spots of higher remaining D content, which can be connected to features in the topography. The crater edge shows a transition width of about 50 µm.

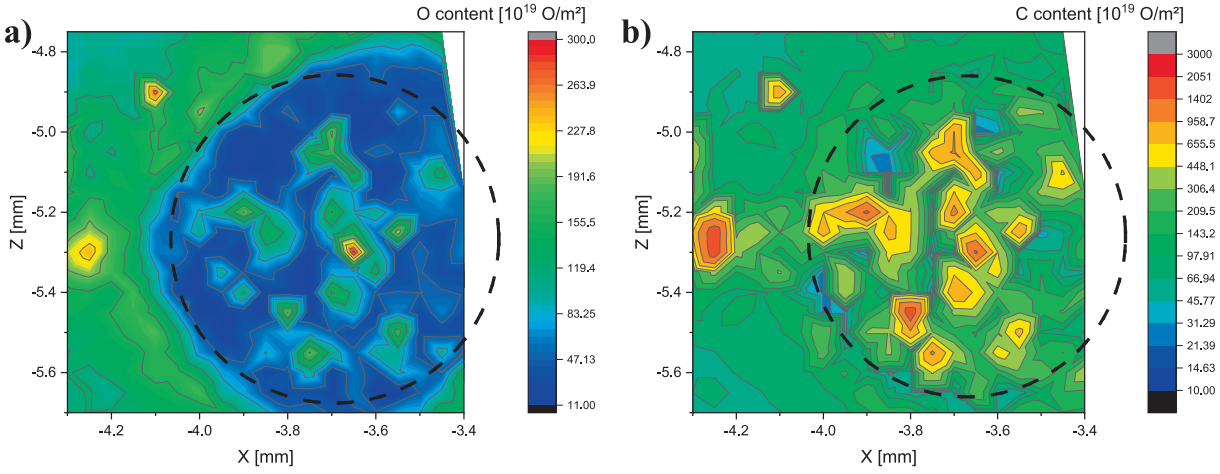

Fig. 6. a) Near-surface o content probed by the $^{16}O(^{3}He,p_0)^{18}F$ reaction with 50 µm lateral resolution. The laser spot is clearly removing the oxygen deposited in the PSI-2 plasma exposure, but some oxygen-rich particulates seem to be deposited by the laser. The Oxygen removal does not follow the laser spot (circle) exactly. b): Logarithmic plot of the C content probed by $^{12}C(^{3}He,p)^{14}N$ with 50 µm lateral resolution. The initially low carbon content of about $0.5 \times 10^{21} C/m^2$ is related to the PSI-2 exposure. In the Laser crater, the C content is significantly increased, but the distribution is focused on a few thick deposits. Some deposits can be found outside the laser area (circle). The maximum at X = -4.25 mm and Z = -5.25 mm is also visible in the topography shown Fig. 5.

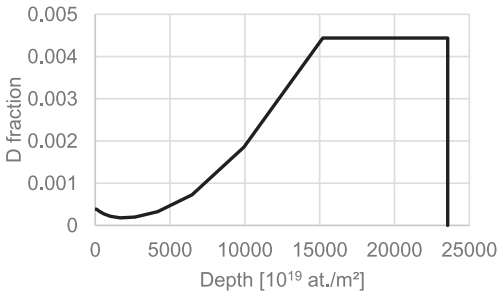

Fig. 7. IBA analysis of the D fraction EDP at the floor of a laser crater. The laser enables a diffusion into the bulk, but also outgasses a part of the diffused D. This graph enables determining the halo effect, since this depth was originally without D. The FWHM depth of the transition is 1.8 µm in W.

to be scaled up by 52% in order to compensate these systematic effects. The relative uncertainty for comparing different LIA results of the same sample is significantly smaller, since we saw e.g. similar circularity deviations in different spots, enabling to cancel most systematic contributions for a relative analysis. From the comparison of three craters, we see variations of a factor 2 in the remaining D fraction. With only 17% remaining fraction, we estimate a 9% relative uncertainty, highlighting the strength of the LIA method as a tool for investigating and comparing processes.

While an absolute quantification would require deepening the understanding of the effects described here, the relative uncertainty is excellent. This is typical for matrix-effect limited methods and makes LIA a very powerful tool when combined with a post-mortem calibration through a method such as IBA. An in-situ calibration, e.g. when the samples vary or a post-mortem sample cannot be extracted from a nuclear environment, appears to be possible in view of the presented data.

A significant fraction of the matrix effect of LIA is related to thermal effects. The present understanding of thermal outgassing might enable a robust subtraction of these effects to reduce the matrix effect towards a reference free LIA analysis with a total accuracy of ≈ 10%.

CRediT authorship contribution statement

Sören Möller: Writing – review & editing, Writing – original draft, Visualization, Validation, Methodology, Investigation, Formal analysis, Data curation, Conceptualization. **Christoph Kawan:** Writing – review & editing, Investigation. **Marcin Rasinski:** Investigation. **Gennady Sergienko:** Writing – original draft, Visualization, Investigation, Formal analysis, Data curation. **Arkadi Kreter:** Resources. **Eduard Grigore:** Resources. **Erik Wüst:** Writing – review & editing, Investigation. **Khoirul Faiq Muzakka:** Software. **Sebastijan Brezinsek:** Resources.

Declaration of competing interest

The authors declare that they have no known competing financial interests or personal relationships that could have appeared to influence the work reported in this paper.

Data availability

Data will be made available on request.

References

[1] V. Palleschi, Laser-induced breakdown spectroscopy: principles of the technique and future trends, ChemTexts 6 (2) (2020) 18, https://doi.org/10.1007/s40828-020-00114-x.
[2] J. Thomas, H. Chandra Joshi, Review on laser-induced breakdown spectroscopy: methodology and technical developments, Appl. Spectrosc. Rev. 59 (1) (2024) 124–155, https://doi.org/10.1080/05704928.2023.2187817.
[3] S. Möller, M. Finsterbusch, K.F. Muzakka, MeV Ion beam analysis of granite in 10000 points', Zenodo, 17, 2024. doi: 10.5281/zenodo.13944189.
[4] M. Mayer, et al., Ion beam analysis of fusion plasma-facing materials and components: facilities and research challenges, Nucl. Fusion 60 (2) (2019) 025001, https://doi.org/10.1088/1741-4326/ab5817.
[5] B. Wielunska, M. Mayer, T. Schwarz-Selinger, A.E. Sand, W. Jacob, Deuterium retention in tungsten irradiated by different ions, Nucl. Fusion 60 (9) (2020) 096002, https://doi.org/10.1088/1741-4326/ab9a65.
[6] A. Kreter, et al., Linear plasma device PSI-2 for plasma-material interaction studies, Fusion Sci. Technol. 68 (1) (2015) 8–14, https://doi.org/10.13182/FST14-906.
[7] H.J. van der Meiden, et al., Monitoring of tritium and impurities in the first wall of fusion devices using a LIBS based diagnostic, Nucl. Fusion 61 (12) (2021) 125001, https://doi.org/10.1088/1741-4326/ac31d6.
[8] S. Möller, et al., A new high-throughput focused MeV ion-beam analysis setup, Art. no. 1, Instruments 5(1) (2021), https://doi.org/10.3390/instruments5010010.
[9] M. Mayer, SIMNRA User's Guide, p. 67, 1997.
[10] K.F. Muzakka, et al., Analysis of Rutherford backscattering spectra with CNN-GRU mixture density network, Sci. Rep. 14 (1) (2024) 16983, https://doi.org/10.1038/s41598-024-67629-y.
[11] T. Genieys, M. Sentis, O. Utéza, Investigation of ultrashort laser excitation of aluminum and tungsten by reflectivity measurements, Appl. Phys. A 126 (4) (2020) 263, https://doi.org/10.1007/s00339-020-3440-9.